THE CFD ANALYSIS OF THE EFFECT OF INTERNAL PEAK ANGLE AND MASS-FLOW RATES ON THE THERMAL PERFORMANCE OF SOLAR AIR HEATER WITH TRIANGLE CROSS-SECTION

by

Walid BEN AMARA [a], ***Yashar ARYANFAR*** [b], ***Hasan KOTEN*** [c*], ***Abdallah BOUABIDI*** [a,d], ***Mouldi CHRIGUI*** [a], ***and Jorge Luis Garcia ALCARAZ*** [e]

[a] Mechanical Modelling, Energy and Material (M2EM), National School of Engineering of Gabes (ENIG), University of Gabes, Gabes, Tunisia
[b] Department of Electric Engineering and Computation, Autonomous University of Ciudad Juarez, Juarez, Chihuahua, Mexico
[c] Mechanical Engineering Department, Istanbul Medeniyet University, Istanbul, Turkey
[d] Higher Institute of Industrial Systems of Gabes (ISSIG), University of Gabes, Gabes, Tunisia
[e] Department of Industrial Engineering and Manufacturing, Autonomous University of Ciudad Juarez, Juarez, Chihuahua, Mexico

Original scientific paper
https://doi.org/10.2298/TSCI220918046A

A new design of solar air heater with triangle cross-section is numerically studied. The thermal performance of solar air heater is studied at various mass-flow rates, inlet air temperatures, and solar irradiation intensities. The CFD model is developed using the software ANSYS FLUENT to study the fluid-flow and heat transfer in the solar air heater. The 3-D discretization is applied to study the thermal performance of solar collector with triangle cross-section. Mesh independence is performed in order to choose the adequate mesh. The discrete ordinate radiation model and the RNG k-ε turbulence model are used to study the radiative heat transfer and the turbulent flow inside the solar air heater. Particularly, effects of different internal peak angles (145°,126°, 100°, 80°, and 67.5°) under different solar irradiation intensities (from 620-1081 W/m²) are studied to improve the thermal performance of the solar air heater. The results show a good agreement between the numerical model and the experimental data with an average error of 6%. The maximum outlet air temperature of the solar air heater reached 72 °C for the geometries with 12 and 16 channels (internal peak angles of 80° and 67.5°, respectively) under mass-flow rate of 0.0264 kg/s. The thermal performances of the solar air heater with 16 and 12 channels are 24.2% higher than standard geometry, respectively for solar irradiation intensity of 1081 W/m². The configuration with internal peak angle of 80° and 12 channels is selected as the optimal with a thermal efficiency of 79%, a low pressure drops compared to geometry with 16 channels and lower costs.

Key words: *solar air heater, CFD, heat transfer, simulation, thermal efficiency*

Introduction

In recent years, the development of thermal systems based on renewable energies has been booming and has been the subject of many works and achievements [1-3]. The particular case of solar collectors continues to develop, improve and become an important part of our dai-

* Corresponding author, e-mail: hasan.koten@medeniyet.edu.tr

ly life since they constitute a very useful category, and they brought an answer to the energetic transformation destined to the applications in the thermal field. The solar air collector is used in many applications requiring low and moderate temperatures: space heating, drying of agricultural products, drying of wood, and drying of bricks [4-7]. Among those research, Koyuncu [8] proposed an experimental investigation on six different flat plate solar collectors to analyze the effect of the number of panes and the shape of the absorber on their efficiency. Findings showed that a collector with single plastic glazing, black painted flat plate absorber and front-pass has a performance of 45.88%. It is approximately 9% more efficient than a collector with double plastic glazing, black painted flat plate absorber and back-pass). Youcef-Ali [9] performed experimental work on a solar collector by introducing thin rectangular plates oriented parallel to the flow direction and welded to the bottom of the absorber. In their work, the authors compared the case of a double-covered collector to a triple-covered collector through experimental designs. They concluded that the triple-covered solar collector reduces heat loss to the front and has a higher thermal performance than the double-covered solar collector. According to the literature, the thermal performance of solar air heater (SAH) is still relatively low. Despite the various merits of solar air collectors, they require further research to improve their thermal efficiencies [10-31]. The CFD work consists in improving the heat transfer and minimizing the pressure loss by changing the internal peak angle from 67.5°-145°. Therefore, different configurations of SAH (3, 5, 8, 12, and 16 channels) are studied under different solar irradiation intensities in order to choose the optimal geometry that gives the highest thermal performances and lowest pressure loss.

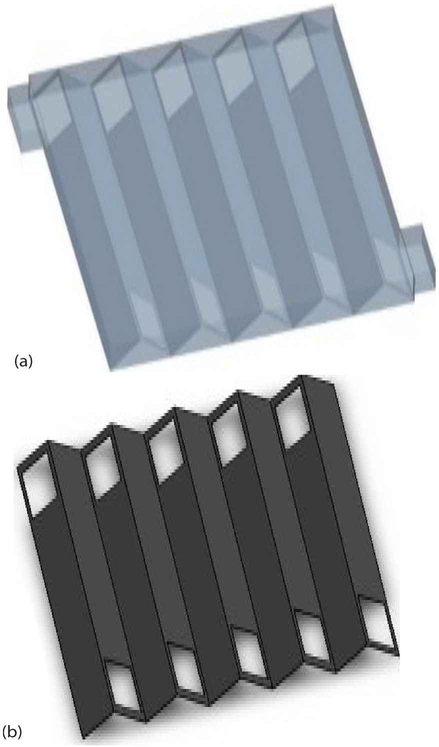

Figure 1. The 3-D geometry of the solar air heater; (a) 3-D computational domain and (b) geometry of the absorber plate

Computational details

Geometry

The geometry and the different views of the SAH with triangle cross-section are shown in figs. 1 and 2. The absorber plate shown in fig. 1(b) comprises 10 copper sheets with dimensions of 1010 mm length, 121.1 mm width, and 2 mm height. The sheets were welded together in a triangular shape at an angle of 27° to the flow path and 126° to the other sheet before being mounted in the solar collector. There are rectangular-shaped holes of 100 mm × 170 mm on each copper sheet to make the fluid pass through the channels.

Governing equations and thermal analysis of SAH

Continuity equations:

$$\nabla(\rho V) = 0 \tag{1}$$

Momentum equations:

$$\nabla(\rho VV) = -\nabla P + \nabla\left[\mu\left(\nabla V - \frac{2}{3}\nabla VI\right)\right] \tag{2}$$

Energy equations:

$$\nabla(\rho VH) = \nabla(K_f \nabla T) \tag{3}$$

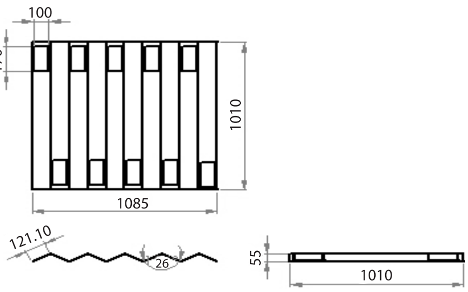

Figure 2. The different views

Grid independence and boundary conditions

Four meshes are tested to verify the independence of the solution are shown in fig. 3. The different details of mesh such as the number of elements and nodes, the size of elements and the maximum skewness are illustrated in tab. 1. The Meshes 3 and 4 tends towards the exact solution found by the experimental test (335 K) with small difference. The Mesh 3 with 572853 elements, is selected as optimal, since it gives the same experimental results, a small storage size and a low calculation time compared to Mesh 4.

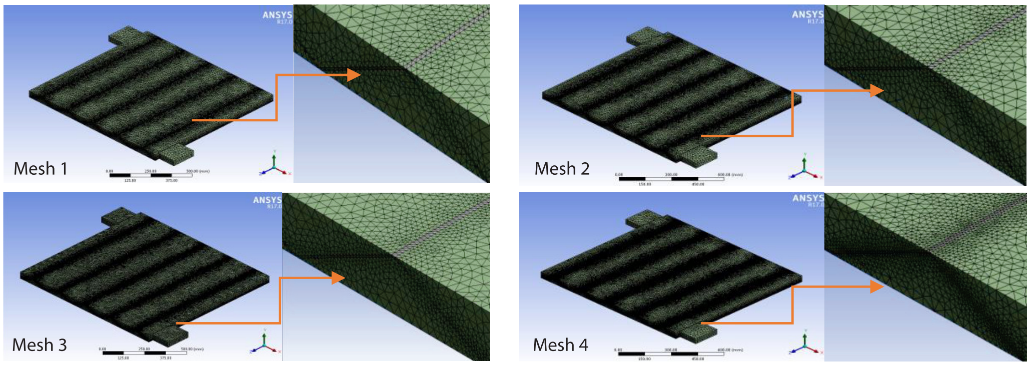

Figure 3. Pictorial views of the mesh model with different numbers of grids

Table 1. Mesh parameters

Grids	Mesh 1	Mesh 2	Mesh 3	Mesh 4
Number of nodes	1276642	1971633	3238611	5969174
Number of elements	231324	352384	572853	1042422
Element size of the fluid domain [mm]	18	16	14	14
Element size of the solid domain [mm]	8	6	6	4
Max. skewness [%]	82	94	97.8	98.2

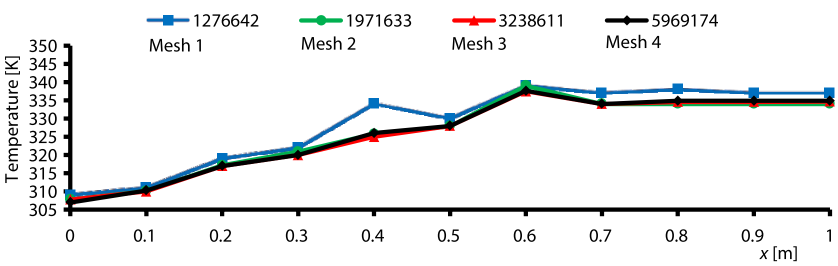

Figure 4. Grid independence analysis for the SAH

The numerical resolution of the adopted mathematical model is conditioned by the initial and boundary conditions applied to the SAH are shown in tab. 2. The 3-D computational domain is divided into four boundaries in fig. 5: inlet, outlet, absorber, and insulated walls. At the inlet of the duct, a mass-flow rate condition is applied, and velocity values are calculated from the Reynolds number, where the mass-flow rate value is 0.0264 kg/s. The sidewalls are considered insulated, and no-slip boundary wall condition is considered.

Table 2. Different values of irradiation intensity and ambient temperature

Irradiation [Wm^{-2}]	Inlet temperature [K]	Mass-flow rate [kgs^{-1}]
620	304.25	0.0264
863	305.75	
1015	307.75	
1081	310.15	
1076	308.95	

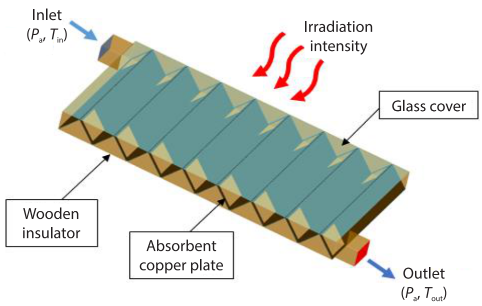

Figure 5. Boundary conditions applied to the collector

The RNG *k-ε t*urbulence can reasonably predict heat transfer and fluid-flow variation and can provide good numerical results in a 3-D conduit [32].

Validation of CFD model

Figure 6 shows the variation of the numerical results of the Nusselt number as a function of different Reynolds number compared with the standard correlation of the Dittus-Boelter equations:

$$\mathrm{Nu} = 0.023\,\mathrm{Re}^{0.8}\,\mathrm{Pr}^{0.4} \tag{4}$$

For different numbers of Reynolds, it notices a good numerical results compared with the correlation of Dittus-Boelter with an average difference do not exceed 6.2%. Figure 7 shows the outlet temperature variation of the collector as a function of solar radiation intensity with a constant mass-flow rate of 0.0264 kg/s. The temperature at the collector outlet increases progressively as the radiation intensity increases until it reaches a maximum at noon of about 65 °C when the radiation intensity is very high. All the numerical and experimental values of the outlet temperature for the solar collector are represented in tab, 3. Also, a good agreement is very remarkable in the fig. 3 between the numerical results using ANSYS FLUENT code and the experimental results of [21], with an error is generally low that does not exceed 6%.

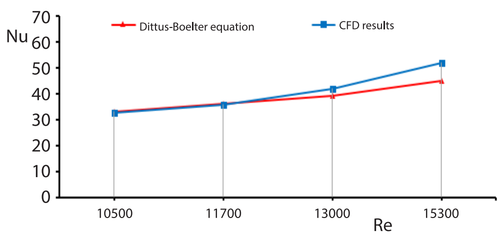

Figure 6. Validation of numerical modelling with verified correlations

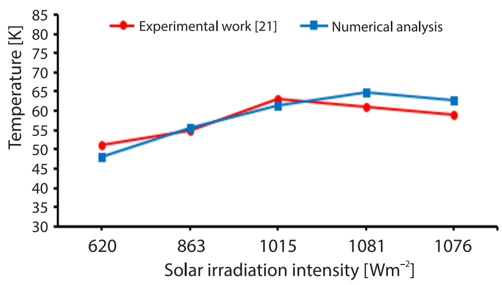

Figure 7. Temperature profiles at the outlet of SAH

Table 3. Values of the outlet temperature for the solar air heater

Irradiation [Wm^2]	Experimental results [21]	Numerical results
620	51 °C	48 °C
863	55 °C	55.5 °C
1015	63 °C	61.4 °C
1081	61 °C	65 °C
1076	59 °C	63 °C

Results and discussion

Effect of different mass-flow rates

The purpose of this study is to increase the surface of thermal exchange between the absorber plate and the fluid in order to improve the thermal efficiency of SAH.

Velocity distribution

Figure 8 illustrates the velocity contours of a SAH. For different mass-flow rates, an ambient temperature equal to 310.15 K and solar radiation equal to 1081 W/m^2. It is notice a strong acceleration in the middle of the collector and near the heated wall. When the fluid changes direction of flow in a helical way, an important increase of the speed where it can reach 10 m/s when switching from one channel to another. Since the flow rate is low, the low speed is noticeable, especially in fig. 8(d), which does not exceed 4 m/s. Also, it can see near the absorbing plate and the external walls that the velocity becomes null because of the non-slip condition.

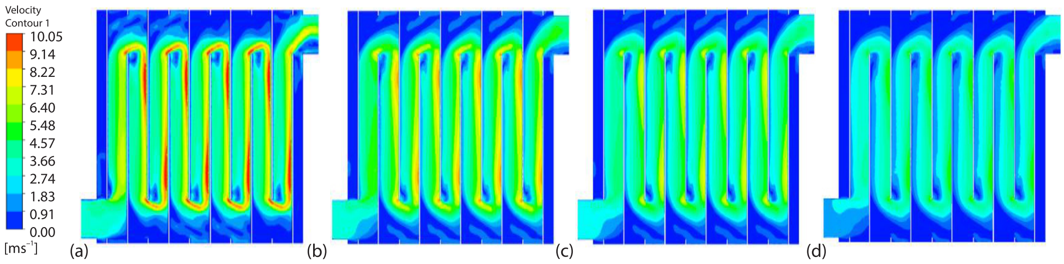

Figure 8. Velocity distribution with different mass-flow rates and radiation intensity equal to 1081 W/m^2; (a) 0.0264 kg/s, (b) 0.022 kg/s, (c) 0.020 kg/s, and (d) 0.018 kg/s

Velocity fields

Plotted in fig. 9, is the distribution of velocities vectors and the SAH with different mass-flow rates. An ambient temperature was 310.15 K, and radiation intensity was 1081 w/m^2. As we know, the distribution of vectors is not almost the same for different mass-flow rates. The distribution of the vectors varied when the mass-flow rate changed from 0.0264-0.018 kg/s. The vectors become null when they contact the walls, and they become very important when the cross-section changes. Also, there are turbulence zones at the exit of each passage that is very noticeable in the zoom of the vectors that slow down the velocity of the fluid.

Pressure contours

Figure 10 shows the relative pressure contours inside the channels for different mass-flow rates with the same initial conditions: radiation intensity equal to 1081 W/m^2, inlet temperature equal to 310.15 K and gauge pressure equal to 0. It can be observed, when the fluid

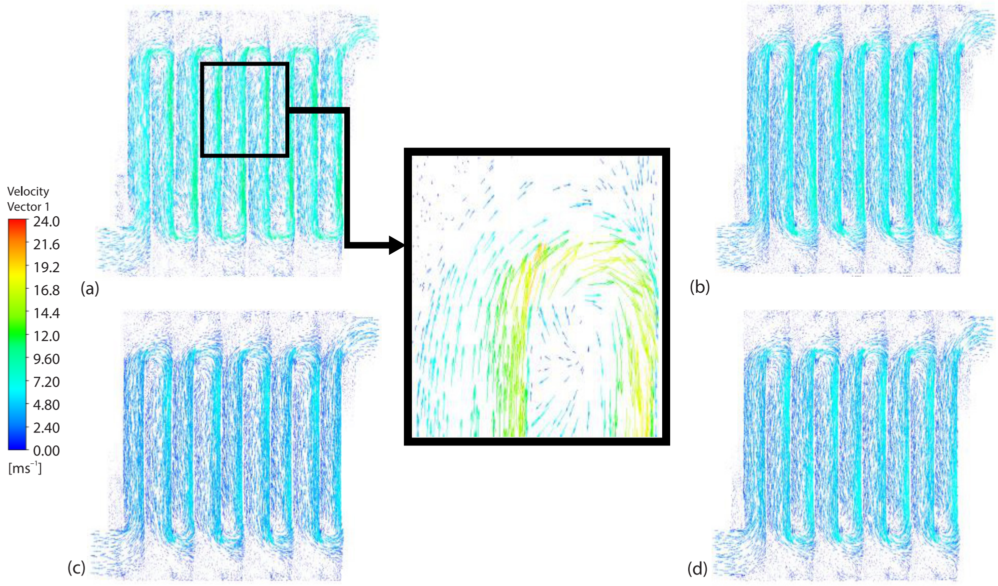

Figure 9. Velocity vector contour for the reference geometries under different mass-flow rates; (a) 0.0264 kg/s, (b) 0.022 kg/s, (c) 0.020 kg/s, and (d) 0.018 kg/s

changes the direction of flow in a helical way, a drop in pressure for all the contours where the relative pressure reaches at the exit of the collector – 348 Pa for an important mass-flow. When the temperature increases, the molecules of the fluid move apart, and the density decreases. Also, by comparing the contours with different mass-flows, it is very clear that the pressure loss decreases from 348-145 Pa when the velocity decreases because of the diminution of the frictional forces.

Temperature contours

Figure 11 shows the temperature field distribution in the XY plane for a solar radiation intensity equal to 1081 W/m^2 with different mass-flow rates: 0.0264 kg/s, 0.022 kg/s, 0.020 kg/s, and 0.018 kg/s. The results show that the air temperature increases progressively from the inlet to the outlet for different mass-flow rates. When we have decreased the mass-flow rates from 0.0264-0.018 kg/s, we notice that the temperature of the collector output decreases from 342-351.70 K. The two red areas in the contour where the temperature is very high (can reach 375 K) is because the velocity of the fluid is zero.

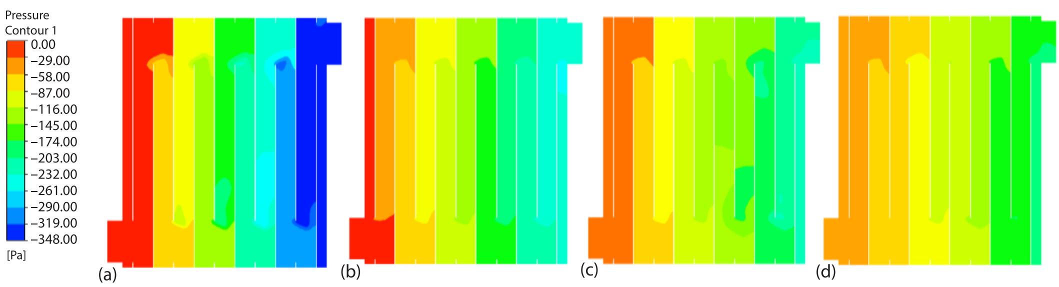

Figure 10. Pressure contours with different mass-flow rates under solar radiation intensity of 1081 W/m^2; (a) 0.0264 kg/s, (b) 0.022 kg/s, (c) 0.020 kg/s, and (d) 0.018 kg/s

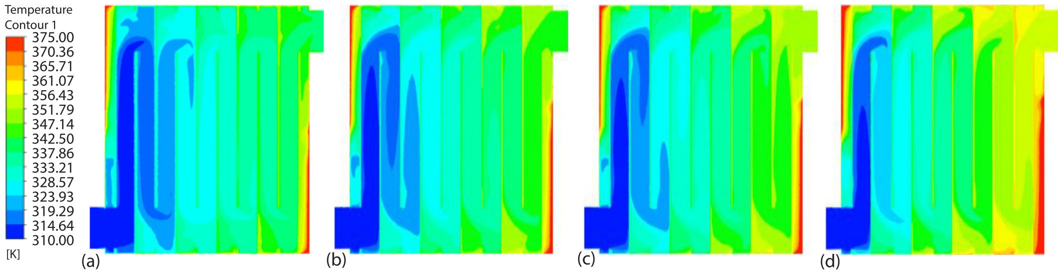

Figure 11. Temperature contours for different mass-flow rates; (a) 0.0264 kg/s, (b) 0.022 kg/s, (c) 0.020 kg/s, and (d) 0.018 kg/s

Temperature profile

Figure 12 shows the solar collector outlet temperature profiles for different mass-flow rates as a function of the incident solar radiation intensity. We observe that the difference between the curves is very noticeable when changing the mass-flow rate from 0.0264-0.018 kg/s, which gives a very high outlet temperature. When the radiation intensity is high, it reaches 352 K at midday for a mass-flow equal to 0.018 kg/s.

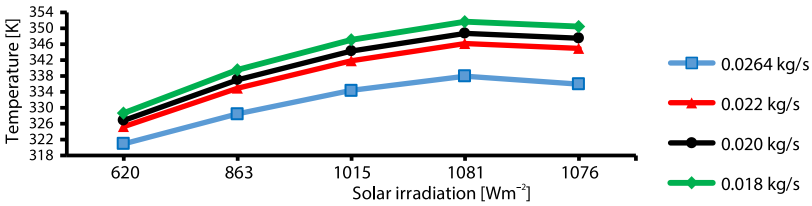

Figure 12. Output temperature profiles of the collector under different mass-flow rates

Effect of internal peak angle

The purpose is to increase the heat exchange surface between the absorber plate and the fluid in order to maximize the thermal performance of the SAH. Figure 13 shows the geometries of SAH with different numbers of channels for the same dimensions: geometry fig. 13(a)

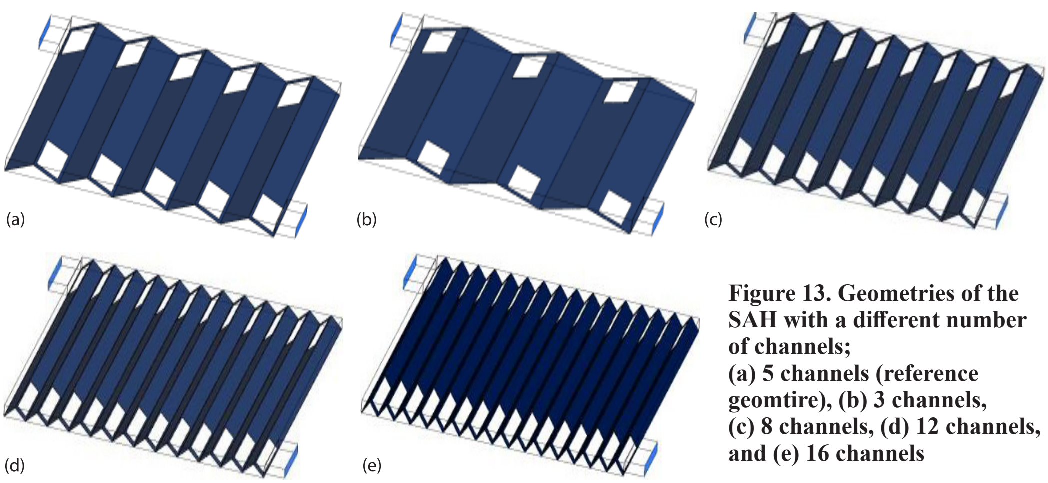

Figure 13. Geometries of the SAH with a different number of channels;
(a) 5 channels (reference geomtire), (b) 3 channels, (c) 8 channels, (d) 12 channels, and (e) 16 channels

was the reference geometry with 5 channels and an internal peak angle equal to 126° and the geometries figs. 13(b)-13(e) with numbers of channels are equal to 3, 8, 12, and 16, respectively, with internal peak, angles were 145°, 100°, 80°, and 67.5° receptivity. All the parameters are shown in tab. 4.

Table 4. Geometric parameters of the channels

Geometry	Numbers of channels	Internal peak angles
Figure 13(a)	5	126°
Figure 13(b)	3	145°
Figure 13(c)	8	100°
Figure 13(d)	12	80°
Figure 13(e)	16	67.5°

Velocity distribution

Figure 14 illustrates the velocity contours of a SAH with a mass-flow rate equal to 0.0264 kg/s, an ambient temperature equal to 310.15 K, and solar radiation equal to 1081 W/m^2. We notice a strong acceleration in the middle of the collector and near the heated wall for all geometries. In figs. 14(d) and 14(e), we can see that the velocity can reach 20 m/s when switching from one channel to another, but fig. 14(b) does not exceed 6 m/s because the passage section is very large compared to the other sections.

Velocity fields

The distribution of velocity vectors is not uniform inside the collector, which is represented in fig. 15. When the fluid changes flow direction in a helical way, an increase of velocity for all the contours is observed, where the velocity vectors can reach 24 m/s for the geometry with 16 channels (with 67.5° internal peak angle). Comparing the contours with the same mass-flow rates equal to 0.0264 kg/s makes it very clear that the velocity of vectors increases when the number of channels increases (the internal peak angle decreases from 145-67.5°) due to the decrease of the passage section. Also, there is the presence of vortex zones when the fluid passes from one channel to another.

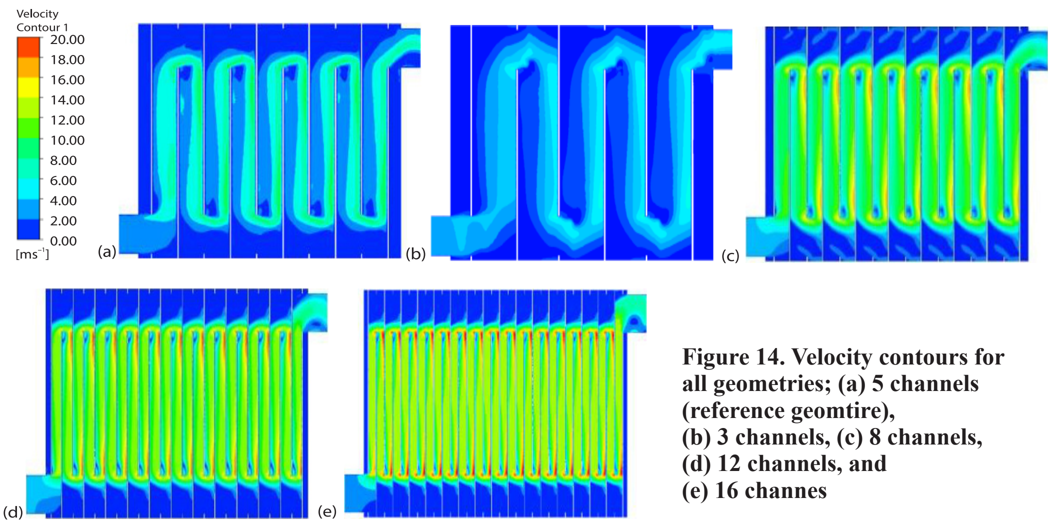

Figure 14. Velocity contours for all geometries; (a) 5 channels (reference geomtire), (b) 3 channels, (c) 8 channels, (d) 12 channels, and (e) 16 channes

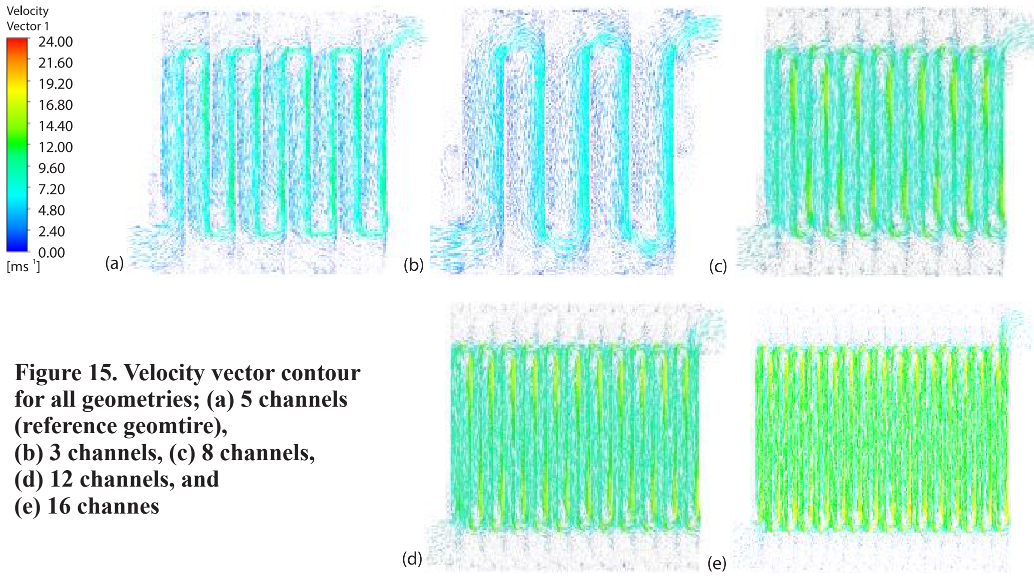

Figure 15. Velocity vector contour for all geometries; (a) 5 channels (reference geomtire), (b) 3 channels, (c) 8 channels, (d) 12 channels, and (e) 16 channes

Pressure contours

Figure 16 shows the pressure distribution inside the SAH for the different geometries under solar irradiation intensity of 1081 W/m^2 and mass-flow rate of 0.0264 kg/s. The air relative pressure decreases as the internal peak angle changes from 145-67.5°, *i.e.*, when the number of channels increases from 3-18 channels. According to fig. 16(b), the pressure drop is very low and does not exceed 226 Pa is due the air particles do not undergo a great resistance during its passages in the channels with large section. As the number of channels increases, the contact surface between the fluid and the internal walls increases, which causes linear pressure losses (friction) and singular pressure losses. The depression is clearly shown in fig. 16(e), where the pressure drops to 622 Pa in the medium.

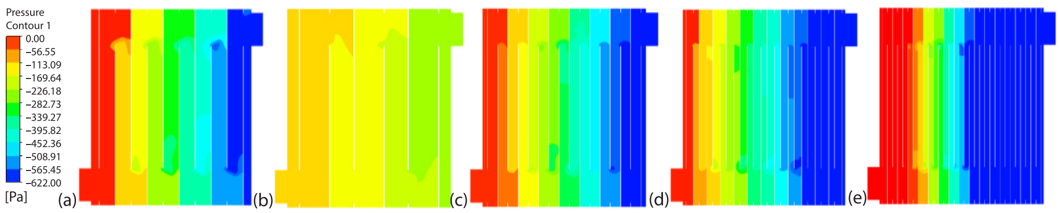

Figure 16. Pressure contours with a mass-flow rate equal to 0.0264 kg/s and radiation intensity equal to 1081 W/m^2; (a) 5 channels (reference geomtire), (b) 3 channels, (c) 8 channels, (d) 12 channels, and (e) 16 channes

Temperature distribution

Figure 17 shows the solar air heater's temperature contours for different geometries obtained by CFD simulation, with a mass-flow rate equal to 0.0264 kg/s, the inlet temperature is 310.15 K, and irradiation intensity is 1081 w/m^2. The air temperature increases progressively during the passage inside the SAH for all contours. Also, the red areas in all the figures representing a high temperature reaching 375 K are caused by the cancellation of fluid velocity as it enters a closed area. In comparison, the difference in the temperature distribution between the five contours is very noticeable. As shown in fig. 17(b), the air temperature increases slowly and does not exceed 340 K at the outlet of the solar air collector, which is almost the same as the outlet temperature of the reference geometry. In figs. 17(c)-17(e), the outlet temperature is higher compared to the fig. 17(a) (the reference geometry); they exceed 345 K, and it can be observed that the fluid temperature of the collector stays constant for the figs. 17(c)-17(e) with 8, 12, and 16 channels, respectively.

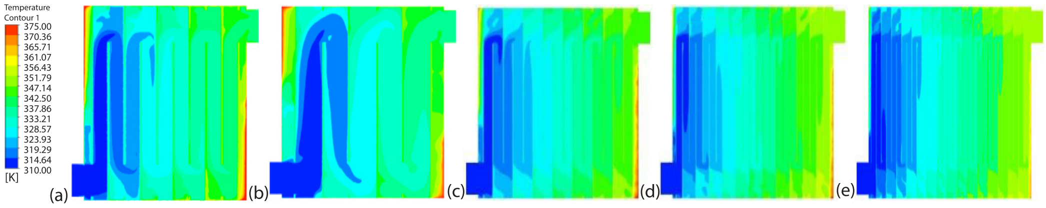

Figure 17. Temperature contours for all geometries with the same mass-flow rates; (a) 5 channels (reference geomtire), (b) 3 channels, (c) 8 channels, (d) 12 channels, and (e) 16 channes

Figure 18 shows the solar collector outlet temperature profiles for all geometries as a function of the different solar radiation intensities. It is observed that the difference between the curves is small when the solar flux is low. On the other hand, at noon, when the intensity of solar radiation is very important, the difference becomes remarkable.

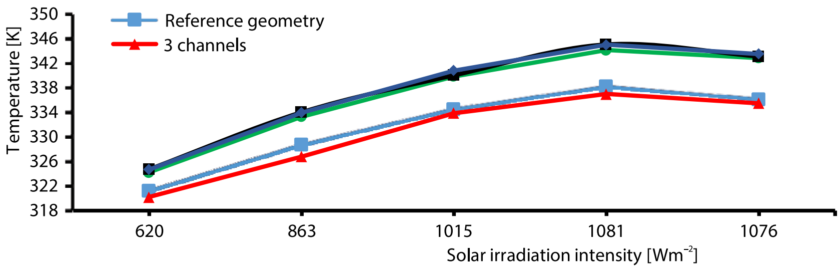

Figure 18. The profiles for the outlet temperature of the solar air heater with different solar radiation intensities

Thermal efficiency variation

Figure 19 shows the variation of thermal efficiency for different configurations under a mass-flow of 0.0264 kg/s and different solar irradiation intensities. It is observed that the thermal performances of all configurations increases with the increase in the number of channels from 3-16 (reduction of the internal peak angle from 145-80°). Comparing the results for all solar irradiation intensities, it is notice that the thermal efficiency for the configurations with 8, 12, and 16 channels higher than the geometry of Haydari *et al.* [21]. This is due to a better heat transfer on account of the increased heat transfer surface by decreasing the internal peak angle. In terms of values, the thermal performances of the SAH with 16, 12, and 8 channels are 34.9%, 34,8%, and 23% higher than SAH with 5 channels [18] for solar irradiation intensity of 1081 W/m^2. Furthermore, the maximum efficiency is found for the geometry with internal peak angle of 80° (12 channels) and it reaches 79.8% and the average efficiency is 78% under mass-flow rate of 0.0264 kg/s. Moreover, it is notice the geometries with 16 and 12 channels generally give the same thermal efficiencies for solar irradiation intensity varied from

620-1081 W/m^2 under mass-flow rate of 0.0264 kg/s. Table 5 summarizes the thermal efficiencies of different types of solar air collectors. It can see that the configuration proposed in this study (with 12 channels) gives a better thermal performance compared to the configurations of the other studies. This is due to the importance of using a V-shaped absorber with internal peak angle of 80° which increases the heat exchange surface.

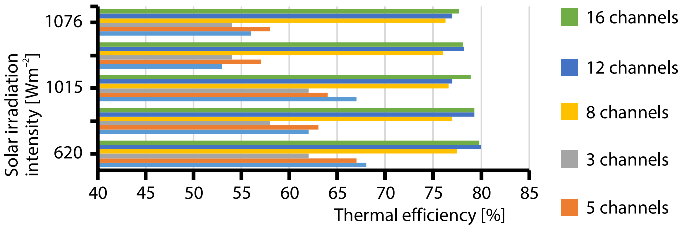

Figure 19. Comparative variation of thermal efficiency of different configurations under different mass-flow rates

Table 5. Summary of some studies about different types of solar air heaters

Authors	Type	Dimensions of the collector	Mass-flow rate	Thermal efficiency
[28]	Double-pass counter flow SAH with V-grooved absorber plate	2 m × 1 m	0.02-0.09 kg/s	40-74%
[13]	Double pass V-corrugaed plate SAH	1 m × 1 m	0.01-0.06 kg/s	52-66%
[29]	A double pass SAH with helical flow path with ratio of $\alpha_1/\alpha_2 = 0.8$	1.085 m × 1.01 m	0.016 kg/s	57-86%
[33]	Single-pass SAH with corrugated absorber	0.7 m × 0.7 m	0.02-0.05 kg/s	5-55%
[34]	Single-pass SAH with wavy absorber plate	1.52 m × 0.52 m	0.0039-0.0118 kg/s	26-38%
[35]	Single-pass SAH with flat plate black coated (solar intensity varied from 400 to 900W/m^2)	2 m × 1 m	0.1324 kg/s	22-40%
[21]	The SAH with helical flow path (solar intensity varied from 620-1085W/m^2)	1.085 m × 1.01 m	0.0264 kg/s	52-77%
This study	Triangle cross-section SAH with different internal peak angles (solar intensity varied from 620-1085W/m^2)	1.085 m × 1.01 m	0.0264 kg/s	54-79.8%

Conclusion

In this work, the thermal performance of a SAH with triangle cross-section is studied numerically. The numerical model is validated against the experimental data and the average error does not exceed 6%. The effect of different internal peak angles (145°, 126°, 100°, 80°, and 67.5°) on the thermal performance of SAH are investigated numerically under different solar irradiation intensities varies from 62-1081 W/m^2 and mass-flow rate of 0.0264 kg/s. The velocity distribution, pressure contours and the air temperature inside the SAH are presented. The maximum air temperature of SAH reaches 72° for both configurations with internal peak angle of 80° and 67.5°. The thermal efficiency of geometry with 12 channels (internal peak angle of 80°) is 24.2% higher than standard SAH under a mass-flow of 0.0264 kg/s and solar irradiation intensity of 1081 W/m^2. Despite their high thermal performance, the geometries with triangle cross-section are complex which causes a significant pressure loss and needed to improve the geometric parameters in order to minimize pressure drops.

References

[1] Hoseinzadeh, S., et al., Using Computational Fluid Dynamics for Different Alternatives Water Flow Path in a Thermal Photovoltaic (PVT) System, *International Journal of Numerical Methods for Heat and Fluid-Flow*, *31* (2021), 5, pp. 1618-1637
[2] Nasrin, R., et al., Effect of Nanofluids on Heat Transfer and Cooling System of the Photovoltaic/Thermal Performance, *International Journal of Numerical Methods for Heat and Fluid-Flow*, *29* (2019), Apr., pp. 1920-1946
[3] Ceviz, M. A., Computational Fluid Dynamics Simulation and Experimental Investigation of a Thermoelectric System for Predicting Influence of Applied Voltage and Cooling Water on Cooling Performance, *International Journal of Numerical Methods for Heat and Fluid-Flow*, *33* (2022), 1, pp. 241-262
[4] Xie, G., *et a*l., Computational Fluid Dynamics for Thermal Performance of a Water-Cooled Minichannel Heat Sink with Different Chip Arrangements, *International Journal of Numerical Methods for Heat and Fluid-Flow*, *24* (2014), 4, pp. 797-810
[5] Ergun, A., Eyinc, H., Performance Assessment of Novel Photovoltaic Thermal System Using Nanoparticle in Phase Change Material, *International Journal of Numerical Methods for Heat and Fluid-Flow*, *29* (2019), 11, pp. 1490-1505
[6] Khanmohammadi,S., *et al.*, Feasibility Study of Using Solar Energy as a Renewable Source in Office Buildings in Different Climatic Regions, *World Journal of Engineering*, *16* (2019), 2, pp. 213-221
[7] Riaz, A., *et al*., Photovoltaic Thermal Building Skin: Effect of Condensing and Evaporating Temperature on Flow Rate and Heat Transfer, *International Journal of Numerical Methods for Heat and Fluid-Flow*, *31* (2021), 6, pp. 1816-1836
[8] Koyuncu, T., Performance of Various Design of Solar Air Heaters for Crop Drying Applications, *Renewable Energy*, *31* (2006), 7, pp. 1073-1088
[9] Youcef-Ali, S., Study and Optimization of the Thermal Performances of the Offset Rectangular Plate Fin Absorber Plates, With Various Glazing, *Renewable Energy*, *30* (2005), 2, pp. 271-280
[10] Gao, W., *et a*l., Analytical and Experimental Studies on the Thermal Performance of Cross-Corrugated and Flat-Plate Solar Air Heaters, *Applied Energy*, *84* (2007), 4, pp. 425-441
[11] Ozgen, F., *et al.*, Experimental Investigation of Thermal Performance of a Double-Flow Solar Air Heater Having Aluminum Cans, *Renewable Energy*, *34* (2009), 11, pp. 2391-2398
[12] Alta, D., *et al*., Experimental Investigation of Three Different Solar Air Heaters: Energy and Exergy Analyses, *Applied Energy*, *87* (2010), 10, pp. 2953-2973
[13] El-Sebaii, A., *et al*., Investigation of Thermal Performance of-Double Pass-Flat and V-Corrugated Plate Solar Air Heaters, *Energy*, *36* (2011), 2, pp. 1076-1086
[14] Bhushan, B., Singh, R., Thermal and Thermohydraulic Performance of Roughened Solar Air Heater Having Protruded Absorber Plate, *Solar Energy*, *86* (2012), 11, pp. 3388-3396
[15] Fudholi, A., *et al*., Performance and Cost Benefits Analysis of Double-Pass Solar Collector with and without Fins, *Energy Conversion and Management*, *76* (2013), Dec., pp. 8-19
[16] Singh,S., et al., The CFD (Computational Fluid Dynamics) Investigation on Nusselt Number and Friction Factor of Solar Air Heater Duct Roughened with Non-Uniform Cross-Section Transverse Rib, *Energy*, *84* (2015), May, pp. 509-517
[17] Sahar, JA. M., *et al*., Effect of Hydraulic Diameter and Aspect Ratio on Single Phase Flow and Heat Transfer in a Rectangular Micro-Channel, *Applied Thermal Engineering*, *115* (2017), Mar., pp. 793-814
[18] Lakshmi, D., *et al*., Performance Analysis of Trapezoidal Corrugated Solar Air Heater with Sensible Heat Storage Material, *Energy Procedia*, *109* (2017), Mar., pp. 463-470
[19] Amraoui, M. A., Aliane, K., The 3-D Analysis of Air-Flow in a Flat Plate Solar Collector, *Periodica polytechnica Mechanical Engineering*, *62* (2018), 2, pp. 126-135
[20] Fan, W., et al., Is it True that the Longer the Extended Industrial Chain, The Better The Circular Agriculture, A Case Study of Circular Agriculture Industry Company in Fuqing, Fujian, *Journal of Cleaner Production*, *189* (2018), July, pp. 718-728
[21] Heydari, A., Mesgarpour, M., Experimental Analysis and Numerical Modelling of Solar Air Heater with Helical Flow Path, *Solar Energy*, *162* (2018), Mar., pp. 278-288

[22] Singh, D., Exergo-Economic, Enviro-Economic and Productivity Analyses of N Identical Evacuated Tubular Collectors Integrated Double Slope Solar Still, *Applied Thermal Engineering*, *148* (2019), Feb., pp. 96-104
[23] Komolafe, C. A., *et al*., Experimental Investigation and Thermal Analysis of Solar Air Heater Having Rectangular Rib Roughness on the Absorber Plate, *Case Studies in Thermal Engineering*, *14* (2019), 100442
[24] Sajawal, M., *et al*., Experimental Thermal Performance Analysis of Finned Tube-Phase Change Material Based Double Pass Solar Air Heater, *Case Studies in Thermal Engineering*, *15* (2019), 100543
[25] Bensaci, C.-E., *et al*., Numerical and Experimental Study of the Heat Transfer and Hydraulic Performance of Solar Air Heaters with Different Baffle Positions, *Renewable Energy*, *155* (2020), Aug., pp. 1231-1244
[26] Zheng, Z., *et al.*, Thermodynamics and Flow Unsteadiness Analysis of Trans-Critical CO_2 in a Scroll Compressor for Mobile Heat Pump Air-Conditioning System, *Applied Thermal Engineering*, *175* (2020), 115368
[27] Tuncer, A. D., *et al*., Energy-Exergy and Enviro-Economic Survey of Solar Air Heaters with Various Air Channel Modifications, *Renewable Energy*, *160* (2020), Nov., pp. 67-85
[28] Rasham, A. M., *et al*., Thermal Performance of Double-Pass Counter Flow and Double-Parallel Flow Solar Air Heater With V-Grooved Absorber Plate, IOP Conference Series, *Materials Science and Engineering*, *13* (2021), 1076
[29] Mesgar, M., *et al*., Geometry Optimization of Double Pass Solar Air Heater with Helical Flow Path, *Solar Energy*, *213* (2021), Jan., pp. 67-80
[30] Sharma, N. Y., *et al*., The Effect of Flow Obstacles of Different Shapes for Generating Turbulent Flow for Improved Performance of the Solar Air Heater, *Procedia Manufacturing*, *35* (2019), Jan., pp. 1096-1101
[31] Hamdy, H., *et al*., An Experimental Investigation of the Performance of New Design of Solar Air Heater (Tubular), *Renewable Energy*, *37* (2019), 12660
[32] Singh, S., *et al*., Utilizing Circular Jet Impingement to Enhance Thermal Performance of Solar Air Heater, *Renewable Energy*, *154* (2020), July, pp. 1327-1345
[33] Benli, H., Experimentally Derived Efficiency and Exergy Analysis of a New Solar Air Heater Having Different Surface Shapes, *Renew. Energy*, *50* (2013), Feb., pp. 58-67
[34] Debnath, S., *et al*., An Expert System-Based Modelling and Optimization of Corrugated Plate Solar Air Collector for North Eastern India, *Journal Brazilian Soc. Mech. Sci. Eng*., *41* (2019), 273
[35] Aissaoui, F., *et al*., Belloufi, Experimental and Theoretical Analysis on Thermal Performance of the Flat Plate Solar Air Collector, *Int. J. Heat Technol*., *34* (2016), 2, pp. 213-220

Paper submitted: September 18, 2022
Paper revised: December 20, 2022
Paper accepted: december 26, 2022